ACS APPLIED MATERIALS & INTERFACES

www.acsami.org

Research Article

Low-Temperature Plasma-Assisted Catalytic Dry Reforming of Methane over CeO_2 Nanorod-Supported NiO Catalysts in a Dielectric Barrier Discharge Reactor

Md Robayet Ahasan, Md Monir Hossain, Zephyr Barlow, Xiang Ding, and Ruigang Wang*

Cite This: *ACS Appl. Mater. Interfaces* 2023, 15, 44984−44995

Read Online

ACCESS | Metrics & More | Article Recommendations | Supporting Information

ABSTRACT: Nonthermal plasma (NTP)-assisted catalytic dry reforming of methane (DRM) is considered a powerful single-stage reaction mechanism because of its ability to activate normally stable CO_2 and CH_4 at a low temperature under ambient conditions. The thermodynamic barrier of DRM requires a high operating temperature (>700 °C), which can be reduced by nonequilibrium plasma. Herein, we present a method for the wet-impregnation synthesis of CeO_2 nanorod (NR)-supported 5 and 15 wt % NiO catalysts for efficient NTP-promoted DRM with an applied power in the range of 24.9−25.8 W (frequency: 20 kHz), a CH_4:CO_2 feed gas ratio of 100:250 sccm, and a total flow rate of 350 sccm. The presence of NTP dramatically increased the reaction activity, even at 150 °C, which is usually inaccessible for thermally catalyzed DRM. The CH_4 and CO_2 conversion reaches a maximum of 66 and 48%, respectively, at 500 °C with the 15 wt % NiO/CeO_2 NR catalyst, which are much higher than the values obtained for the 5 wt % NiO/CeO_2 NR catalyst under the same conditions. According to the X-ray photoelectron spectroscopy profile for 15 wt % NiO/CeO_2 NR, a higher concentration of NiO on CeO_2 increases the proportion of Ce^{3+} in the catalyst, suggesting enhanced oxygen vacancy concentration with an increased amount of NiO loading. Additionally, a higher NiO loading promotes a higher rate of replacement of Ce^{4+} with Ni^{2+}, which generates more oxygen vacancies due to the induced charge imbalance and lattice distortion within the CeO_2 lattice. As a result, it can be inferred that the incorporation of Ni ions into the CeO_2 structure resulted in inhibited growth of CeO_2 crystals due to the creation of a $Ni_xCe_{1-x}O_{2-\alpha}$ solid solution and the production of oxygen vacancies.

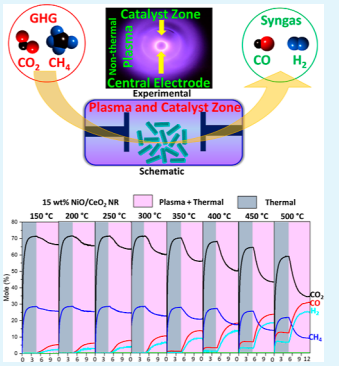

KEYWORDS: *nonequilibrium plasma, nonthermal plasma, dry reforming of methane, nickel, CeO_2 nanorods*

1. INTRODUCTION

Global warming and threatening climatic changes due to the increasing emission rate of greenhouse gases (GHG) have attracted considerable attention from scientists. The dry reforming of methane (DRM) reaction is regarded as a new strategy for simultaneously converting CO_2 and CH_4, two dominant GHGs, into valuable syngas (H_2 and CO) and/or liquid hydrocarbons. In recent years, nonthermal plasma (NTP) has demonstrated itself as a powerful platform due to its ability to induce the highly endothermic DRM reaction shown in eq 1, even at lower temperatures.

$$CH_4(g) + CO_2(g) \rightarrow 2CO(g) + 2H_2(g)$$
$$\Delta H_{298K} = +247\ \text{kJ mol}^{-1} \quad (1)$$

While conventional thermal catalysis of DRM at high temperatures (>700 °C) leads to massive carbon deposition (coking) and catalyst poisoning, plasma with an efficient catalyst showed more significant potential for low-temperature DRM and boasts easy installation, lower cost, and higher efficiency. NTP technology overcomes the thermodynamic barrier of the endothermic DRM reaction at lower temperatures and generates highly energetic species such as electrons, radicals, ions, and metastable species.[1] The coupling of plasma and a catalyst leads to plasma-catalytic synergism that allows for more energy-efficient CH_4 and CO_2 conversion with numerous advantages when compared with conventional thermal catalysis.

Although noble metals such as Ru, Pt, and Rh demonstrate excellent catalytic activity via their C−H bond cracking capability and coke resistance properties, their uneconomical costs prevent them from being used commercially.[2−5] Ni-based catalysts show good catalytic activity of DRM with mild coke resistance comparable with that of many earth-abundant and low-cost transition-metal oxide catalysts, making them promising and suitable for large-scale commercial applications. Khoja et al.[6] reported that a 10 wt % Ni/γ-Al_2O_3−MgO catalyst showed a maximum of 74.5% CH_4 and 73% CO_2

Received: June 28, 2023
Accepted: August 29, 2023
Published: September 13, 2023

https://doi.org/10.1021/acsami.3c09349
ACS Appl. Mater. Interfaces 2023, 15, 44984−44995

conversion in thermal DRM testing, which was attributed to its high Lewis basicity, solid metal−support interaction, dispersion, and stability. Unfortunately, Ni as an active catalyst is still limited to lab-scale research because of the quick deactivation of the active material due to catalyst poisoning from methane decomposition and CO disproportion, as shown in eqs 2 and 3.[7]

$$CH_4(g) \rightarrow C_{ads} + 2H_2(g) \quad (2)$$

$$2CO(g) \rightarrow C_{ads} + CO_2(g) \quad (3)$$

For the DRM reaction, the researcher conducted multiple experiments with Ni-based catalysts supported on metal oxides, including alumina (Al_2O_3), silica (SiO_2), ceria (CeO_2), and zirconia (ZrO_2), or a mixture of two or more of these oxides.[8] Among these supports, CeO_2 received the most attention due to its unique reduction properties, its oxygen storage and release capacity, and its strong metal−support interaction (SMSI). In addition, the defects and oxygen vacancies present in CeO_2 enhance the adsorption and desorption behavior of the catalyst for CO_2 activation as well as facilitate the detachment of carbon from the catalyst surface.[9] Shape-controlled and surface-engineered CeO_2 has found widespread applications in a variety of catalytic fields due to the fact that CeO_2 nanocrystals contain highly reactive surface oxygen vacancies and other defects that promote the reduction of adjacent Ce^{4+} to Ce^{3+}.[10] In the literature, Ni/CeO_2 exhibited superior catalytic activity compared to Ni/α-Al_2O_3, Ni/TiO_2, Ni/ZrO_2, Ni/SiO_2, and Ni/MgO, which was attributed to higher Ni dispersion and a SMSI between NiO_x and CeO_2. SMSI promotes oxygen vacancy formation and enhances surface coverage by CO_2 species.[11] As a result, the interface and interaction of Ni and surface-engineered CeO_2 could be a promising approach for enhancing catalyst stability and promoting anticoking properties. In this work, we prepared 5 and 15 wt % NiO-doped CeO_2 nanorod (NR)-supported catalysts via the wet impregnation method to investigate the effect of NiO deposition with CeO_2 NR on DRM performance in an atmospheric pressure dielectric barrier discharege (DBD) plasma environment. The reason for choosing the 5 and 15 wt % NiO loadings is to establish an adequate understanding of the activity of the supported catalyst across a representative composition range. In the literature, for thermal- and plasma-assisted DRM, numerous scientific papers have reported experimental studies fitting within this specified range.[12−14] In addition, an excess amount of NiO loading over the CeO_2 NR support will result in the formation of bulk NiO, which will weaken the metal−support interaction.[15] X-ray diffraction (XRD), Raman spectroscopy, H_2-temperature programed reduction (H_2-TPR), CO_2-temperature-programed desorption (CO_2-TPD), and X-ray photoelectron spectroscopy (XPS) were used to analyze the morphological and chemical characteristics of catalysts in order to investigate the metal−support interaction and the factors influencing the DRM activities.

2. EXPERIMENTAL SECTION

2.1. Catalyst Preparation. *2.1.1. Materials.* Cerium(III) nitrate hexahydrate [$Ce(NO_3)_3{\cdot}6H_2O$] (99.5% pure) was purchased from Acros Organics. Sodium hydroxide [NaOH] (99% pure) and ammonium hydroxide [$NH_3{\cdot}H_2O$, BDH, 28−30 vol %] were purchased from VWR. Nickel(II) nitrate hexahydrate [$Ni(NO_3)_2{\cdot}6H_2O$] (99.9% pure) from Alfa Aesar was used as the precursor for the Ni catalysts. The chemicals were used without further purification.

2.1.2. Preparation of the CeO_2 NR Support. 3.8403 g amount of $Ce(NO_3)_3{\cdot}6H_2O$ was dissolved in 88 mL of deionized (DI) water to prepare 88 mL of 0.1 M $Ce(NO_3)_3{\cdot}6H_2O$ solution. An 8 mL aqueous solution of 6 M NaOH was prepared by dissolving 1.93 g of NaOH in 8 mL of DI water. Then, 8 mL of 6.0 M NaOH solution was added dropwise to 88 mL of 0.1 M $Ce(NO_3)_3{\cdot}6H_2O$ and mixed vigorously in a 200 mL Teflon autoclave liner. The solution was stirred for 15 s, and then the closed Teflon liner was transferred into a stainless-steel autoclave and sealed tightly. The temperature of the stainless-steel autoclave was maintained at 90 °C for 48 h. Afterward, the autoclave was cooled to ambient temperature, and the obtained precipitate was washed thoroughly with 500 mL of DI water to remove any residual ions (Na^+, NO_3^-). The product was then washed with 50 mL of ethanol and finally dried in air at 60 °C for 12 h to avoid hard agglomeration of the CeO_2 nanoparticles. Then, the dried sample was collected and ground gently with a mortar and pestle.[10,16]

2.1.3. Preparation of NiO/CeO_2 NR Catalysts. NiO/CeO_2 NR catalysts were prepared using a wet impregnation method with two different NiO loadings. 0.95 g of CeO_2 NR powder and 0.85 g of CeO_2 NR powder, respectively, were put into 100 mL of DI water in 200 mL beakers. $Ni(NO_3)_2{\cdot}6H_2O$, equivalent to 5 and 15 wt % Ni, respectively, was added to the suspension solutions of the CeO_2 NR support powders under stirring. The suspension solutions were mixed vigorously using magnetic stirring followed by dropwise addition of 0.5 M aqueous solution of ammonium hydroxide ($NH_3{\cdot}H_2O$, BDH, 28−30 vol %) to maintain the pH value of the suspension to ∼9. The stirring (400 rpm) continued for 4 h at 80 °C. Finally, the precipitates were transferred into a drying oven at 80 °C and kept overnight. A fine powder of the collected samples was obtained using a mortar and pestle and left in an air furnace for calcination at a rate of 10 °C/min up to 350 °C and maintained at this temperature for 5 h. Figure 1 shows the pictorial presentation of the complete NiO/CeO_2 NR catalyst preparation method.

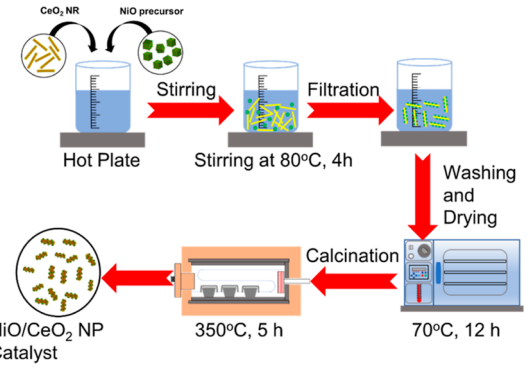

Figure 1. Synthesizing steps of NiO/CeO_2 NR catalysts using a wet impregnation method.

2.2. Catalyst Characterization. The crystal structures of the synthesized catalysts were observed via powder XRD using a Phillips X'Pert MPD diffractometer operated at 40 kV and 40 mA with a copper Kα radiation source (λ = 0.154 nm). Each scanned profile used a 0.5° min^{-1} scan rate with a 2θ range between 10 and 90°. Jade software was used to analyze each catalyst's lattice parameters and average crystal size from the recorded XRD patterns.

The Brunauer−Emmett−Teller (BET) surface area was obtained with a Micromeritics AutoChem II 2920 chemisorption analyzer using a nitrogen adsorption−desorption isotherm at 77 K. The same instrument was used to characterize H_2-TPR and CO_2-TPD. For H_2-TPR analysis, the powder samples (85−95 mg) were placed in a quartz U-tube sandwiched between two pieces of quartz wool and then heated at a rate of 10 °C/min from 30 to 900 °C. During H_2-TPR analysis, the samples were reduced at a flow rate of 50 mL/min in a 10 vol % H_2−90 vol % Ar gas mixture. A thermal conductivity

https://doi.org/10.1021/acsami.3c09349
ACS Appl. Mater. Interfaces 2023, 15, 44984−44995

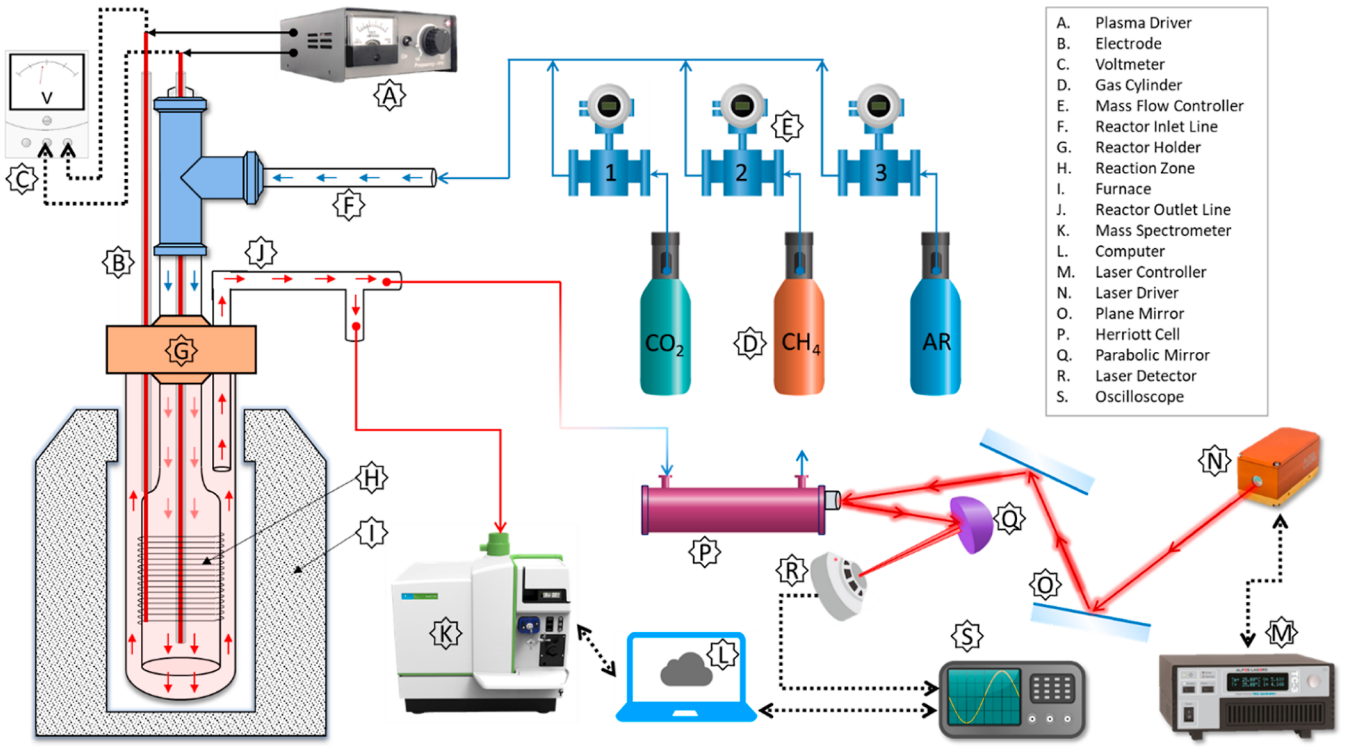

Figure 2. Schematic diagram of the DBD plasma reactor with accessories for DRM.

detector (TCD), which was calibrated using a quantitative reduction of CuO to metallic copper, was used to monitor the quantity of H_2 uptake during the reduction. For the CO_2-TPD analysis, the sample was placed in a quartz U-tube and heated from room temperature to 400 °C with a helium (He) stream (flow rate: 50 mL/min) to remove residual moisture. After the system was cooled to room temperature, 10 vol % CO_2−90 vol % He mixture gas was supplied with a flow rate of 50 mL/min through the sample for 60 min. The sample was then heated to 900 °C at a linear ramping rate of 10 °C/min under He gas. A TCD was used to evaluate the desorption behavior of CO_2 at elevated temperatures.

High-resolution transmission electron microscopy (HRTEM) images were obtained using an FEI Tecnai F20 instrument with an acceleration voltage of 200 kV to observe microstructures. A JEOL 7000 FE SEM instrument was used to obtain surface morphology and assess elemental distribution (energy-dispersive X-ray spectroscopy data or EDX). For transmission electron microscopy (TEM) sample preparation, powder samples went through ultrasonic dispersion in ethanol. One or two drops of the suspension solution were deposited on an ultrathin carbon film supported by a 400-mesh copper grid (Ted Pella Inc.) and then dried for 2 h before analysis.

The surface chemical composition of the synthesized samples was measured using a Kratos Axis Ultra DLD spectrometer with a monochromatic Al Kα (hv = 1486.6 eV) source under ultrahigh vacuum (10^{-10} Torr). For XPS analysis, carbon (C) 1s at 284.8 eV was used for calibration of binding energies (BE). The fitting and deconvolution of the spectra were conducted using CasaXPS software.

For nondestructive characterization, Raman experiments of the catalysts were conducted using a HORIBA LabRAM HR 800 Raman spectrometer (equipped with a 100× long working distance objective, NA = 0.60) in the spectral range from 100 to 1200 cm^{-1}. Before each analysis, the spectrometer was calibrated using a single-crystal Si wafer. A diode-pumped solid-state laser system (Laser Quantum MPC6000) tuned at λ = 532 nm was used for excitation.

2.3. Reactor Setup. Figure 2 displays the schematic diagram for the plasma DRM catalyst testing system together with a gas flow diagram and analysis system. The testing system can be divided into three sections: flue gas analysis, the DBD reactor, and the gas supply. CH_4, CO_2, and Ar gases from Airgas (purity >99.99%) are fed to the reactor by mass flow controllers (Brooks GF040 MultiFlo MFC, response time 1 s) in the gas supply section. The DBD reactor consists of two concentric quartz tubes, which are placed inside the furnace (ATS 3210, max. temp. 1200 °C). The outer quartz tube has a constant outer diameter (OD) of 25.4 mm, while the inner quartz tube (OD = 6.35 mm) features an expansion portion (inner diameter = 9.53 mm, length = 50 mm). In order to generate plasma, one electrode (Kanthal A-1 wire, 24 g), which is covered with a ceramic tube, is placed at the center axis of the quartz tubes. Another thin wire (Kanthal A-1 wire, 32 g) is wrapped around the inner tube expansion section as the other electrode. Both electrodes are connected to a plasma generator (PVM/DDR plasma driver). The catalyst material is positioned inside the inner expansion part of this reactor and distributed with quartz wool; the plasma is created in this expansion section.

Flue gases are analyzed in the flue gas analysis system where some gases (CO, H_2, CH_4, CO_2, and Ar) are detected by a mass spectrometer (Extrel QMS, MAX300-EGA, 300 ms, 1−250 amu detectability) and other gases (higher hydrocarbon like C_2H_6) are detected using an infrared (IR) laser absorption spectrometer system. The IR laser absorption spectroscopy portion is a specially designed system that includes a quantum cascade laser (Alpes Lasers, sbcw6200 DN) with a controller and laser supply, a handmade Herriott cell to extend the gas adsorption length, an IR detector (Vigo, PVMI-4TE) to detect laser signals, an oscilloscope (Tektronix TBS1154, 150 MHz) to visualize the signal, and a waveform generator (B&K Precision, 4055B, 1 μHz to 60 MHz) to trigger the laser. The same setup has been used before for the oxidative coupling of methane, and its accuracy was confirmed.[17]

In the DRM analysis, CH_4 and CO_2 were used at a total flow rate of 350 sccm (CH_4/CO_2 molar ratio = 100:250 = 0.4). Ar gas was used to purge or neutralize the reactor from other contaminated gases before starting the experiment for each observation. The catalyst was regenerated using a mixed supply of Ar and CO_2 (Ar/CO_2 molar ratio = 100:250 = 0.4). Each type of gas flow was controlled by a separate MFC and mixed before pumping into the reactor. The reaction zone temperature was regulated using the furnace, where the temperature ranged from 150 to 500 °C with a 4 °C/min ramp, and the plasma supply was controlled manually. The DBD reactor was linked to an

https://doi.org/10.1021/acsami.3c09349
ACS Appl. Mater. Interfaces 2023, 15, 44984−44995

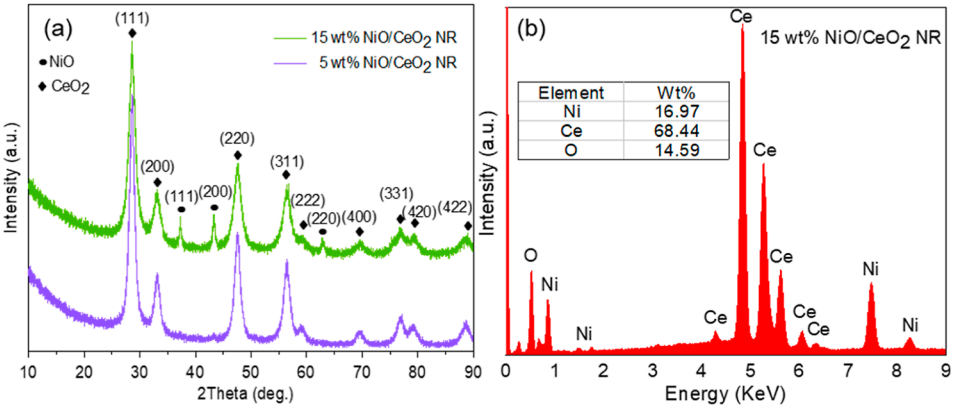

Figure 3. (a) XRD patterns of 5 wt % NiO/CeO_2 NR and 15 wt % NiO/CeO_2 NR and (b) EDS analysis of 15 wt % NiO/CeO_2 NR.

AC high-voltage power supply (PVM500−2500 from http://Amazing1.com) with a peak-to-peak voltage of 40 kV and a frequency of 20−70 kHz. In this work, the power supply frequency was fixed at 20 kHz. The electrical signals (applied voltage and current) were recorded by a four-channel digital oscilloscope (Tektronix, TBS1154) using a high-voltage probe (Tektronix P6015A) and a current transformer (Magnelab, CT-E 0.5 BNC). A discharge power in the range of 24.9−25.8 W was calculated for this work. The gas sample was collected from the reactor in both the QMS and QCL systems, where the flue gas was continuously analyzed and data were logged into the incorporated data acquisition system.

2.4. Performance Parameters. The conversion of CH_4 and CO_2 is expressed as the ratio of the moles of reactants converted to the moles of reactants initially present. The yield of a reaction is the proportion of the desired product produced (in moles) to the maximum possible yield, assuming complete conversion of the limiting reactant and no side reactions. The selectivity refers to the ratio of the desired product formed to the amount of undesired products formed. The equations used for the calculation of conversion, yield, and selectivity in a DRM reaction are presented below

$$C_{CH_4} = \frac{\text{moles of } CH_4 \text{ converted}}{\text{moles of } CH_4 \text{ input}} \times 100\% \quad (4)$$

$$C_{CO_2} = \frac{\text{moles of } CO_2 \text{ converted}}{\text{moles of } CO_2 \text{ input}} \times 100\% \quad (5)$$

$$Y_{H_2}\,(\%) = \frac{\text{moles of } H_2 \text{ produced}}{2 \times \text{moles of } CH_4 \text{ input}} \times 100\% \quad (6)$$

$$Y_{CO}\,(\%) = \frac{\text{moles of CO produced}}{\text{moles of } CH_4 \text{ input} + \text{moles of } CO_2 \text{ input}} \times 100\% \quad (7)$$

$$S_{H_2}\,(\%) = \frac{\text{moles of } H_2 \text{ produced}}{2 \times \text{moles of } CH_4 \text{ converted}} \times 100\% \quad (8)$$

$$S_{CO}\,(\%) = \frac{\text{moles of CO produced}}{\text{moles of } CH_4 \text{ converted} + \text{moles of } CO_2 \text{ converted}} \times 100\% \quad (9)$$

3. CHARACTERIZATION

3.1. X-ray Diffraction. The XRD patterns in Figure 3a exhibit the peaks of the cubic fluorite structure of CeO_2, confirmed by JCPDS# 34−0394, space group $Fm3m$. According to the XRD database and literature, the peaks with 2θ values at 28.5, 33.1, 47.5, 56.3, 59.1, 69.4, 76.7, and 79.1° correspond to the planes (111), (200), (220), (311), (222), (400), (331), (420), and (422), respectively.[18] The results demonstrated that the CeO_2 NRs maintained their crystal structure after the wet impregnation of NiO and calcination at 350 °C for 5 h. The XRD pattern of 5 wt % NiO/CeO_2 NR showed no significant NiO peaks, suggesting that NiO was highly dispersed on CeO_2 NR or that there was a low metal content.[19] As NiO peaks are very weak and mixed with the background, it is nearly impossible to determine the crystal size by using the Scherrer formula. The XRD pattern of 15 wt % NiO-doped CeO_2 had three additional peaks besides the CeO_2 peaks. These XRD peaks had 2θ values of 37.2, 43.2, and 62.8°, which correspond to the (111), (200), and (220) planes of NiO, respectively.[20] Figure 3b depicts the EDS line scanning result of 15 wt % NiO/CeO_2 NR, illustrating the approximate similarity of NiO loading of the prepared sample. The average crystallite size was determined by using the highest peak associated with the CeO_2 (111) plane. Using the Scherrer formula, the average crystallite sizes of 5 wt % NiO/CeO_2 NR and 15 wt % NiO/CeO_2 NR were found to be 8.74 and 7.14 nm, respectively. The reduction of crystallite size was due to the replacement of Ni^{2+} ions (0.055 nm) with Ce^{3+} or Ce^{4+} ions (0.114 or 0.097 nm).[21] As a result, it can be assumed that the integration of Ni ions with Ce ions inhibited the growth of CeO_2 crystals by forming $Ni_xCe_{1-x}O_{2-\omega}$, which is a solid solution with ample oxygen vacancies. Increased NiO loading led to a minor shift in the diffraction peaks of NiO and CeO_2 toward a higher Bragg's angle, indicating the presence of diffusion-made solid solution on the catalyst surface.[22] In the 15 wt % NiO/CeO_2 NR, the peak intensity of NiO increased relative to the background, suggesting probable agglomeration of NiO, as reported by Zhao et al.[19] Their work explored the relationship between higher NiO concentrations and higher intensity of NiO peaks and found that NiO agglomeration can occur when the NiO concentration exceeded 4%.

3.2. H_2-Temperature Programed Reduction. As shown in the H_2-TPR profiles in Figure 4, the three reduction peaks observed for CeO_2 NR at 350, 486, and 745 °C are attributed to the surface reduction (350 and 486 °C) and bulk reduction (745 °C), which are consistent with the literature reports.[23,24] Figure 4 also exhibits three reduction peaks α, β, and γ for 5 wt % NiO/CeO_2 NR and 15 wt % NiO/CeO_2 NR. In general, the reduction peaks of CeO_2-supported NiO catalysts are observed in the temperature range of 200−600 °C.[25] Thus, these high-temperature reduction peaks at 731, 745, and 756 °C for these three samples are ascribed to the bulk reduction of CeO_2 support.[26,27] The addition of NiO has a significant influence on

https://doi.org/10.1021/acsami.3c09349
ACS Appl. Mater. Interfaces 2023, 15, 44984−44995

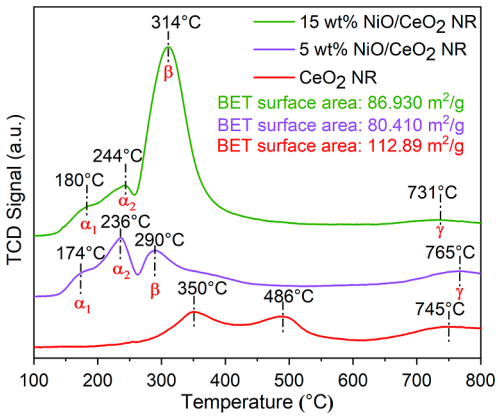

Figure 4. H_2-TPR profiles of pure CeO_2 NR, 5 wt % NiO/CeO_2 NR, and 15 wt % NiO/CeO_2 NR.

the low-temperature surface reducibility (i.e., reduction temperature and hydrogen consumption) of CeO_2, as shown in Figure 4. The low-temperature peaks (α_1 and α_2) observed below 250 °C were caused by the reduction of surface oxygen, which are possibly attached to the oxygen vacancies generated by the partial substitution of Ce^{4+} ions with Ni^{2+} ions. Another peak was observed in the 250−400 °C region, labeled as the β peak for 5 wt % NiO/CeO_2 NR and 15 wt % NiO/CeO_2 NR. The 15 wt % NiO/CeO_2 NR catalyst possessed a distinct β peak with an extra-high intensity when compared to the 5 wt % NiO/CeO_2 NR catalyst. The β peak is attributed to reduction of NiO_x incorporated in the CeO_2 lattice or the Ni−Ce−O solid solution. The solid solution of $Ni_xCe_{1-x}O_{2-\alpha}$ is formed by replacing Ce^{4+} with Ni^{2+}, which generates a charge imbalance and lattice distortions within the CeO_2 lattice, resulting in a high concentration of oxygen vacancies. The solid solution of Ni−Ce−O includes both weak and strong NiO_x/CeO_2 interactions, which govern the reduction of highly dispersed NiO and cause the agglomeration of NiO on the CeO_2 surface as represented by the β peak. Hence, the β peak plays a key role in enhancing the catalytic activity in low-temperature catalytic DRM. In contrast, the γ and α peaks are considered insignificant for catalytic improvement (Table 1).[28]

3.3. X-ray Photoelectron Spectroscopy. XPS was conducted to analyze the surface composition and chemical state of the Ni/CeO_2 catalysts. Figure 5 displays the XPS spectra along with the fitted deconvolution of the 3d orbital of Ce, the 1s orbital of O, and the 2p orbital of Ni for both CeO_2 NR-supported 5 and 15 wt % NiO catalysts, respectively. Figure 5a,d demonstrate the Ce 3d XPS analysis for 5 wt % NiO/CeO_2 NR and 15 wt % NiO/CeO_2 NR. Here, the peaks at 915.5, 906.4, 900.1, 897.5, 886.4, and 881.4 eV are assigned to the Ce^{4+} states, denoted by U‴, U″, U′, V‴, V″, and V′, respectively.[29] The final states of Ce $3d_{3/2}$ and Ce $3d_{5/2}$ are represented by letters U and V, respectively. In contrast, the peaks U° and V° are located at 895.2 and 876.7 eV, respectively, and correspond to Ce^{3+}. It is noted that the peaks at 895.2 and 876.7 eV represent the concentration of the Ce^{3+} state, which is more vital for the 15 wt % NiO/CeO_2 NR catalyst than for the 5 wt % NiO/CeO_2 NR catalyst.[30,31] This is because each Ni ion substitution in the CeO_2 lattice creates an oxygen vacancy with two electrons to make up for the charge difference between Ce^{4+} and Ni^{2+}, leading to the formation of Ce^{3+} ions, which is a key factor that influences the catalytic performance of the DRM reaction.[8] Therefore, it is reasonable to conclude that 15 wt % NiO/CeO_2 NR contains more oxygen defects than 5 wt % NiO/CeO_2 NR. The XPS profiles of the O 1s given in Figure 5b,e strongly support this hypothesis. The peaks were fitted using the Gaussian function at BE = 529.1 and 532.4 eV, respectively, for the $[O]_{Ce}{}^{4+}$ and $[O]_{Ce}{}^{3+}$ oxygen.[32] The oxygen-bound peak for Ce^{3+} is stronger at 15 wt % NiO/CeO_2 NR than at 5 wt % NiO/CeO_2 NR. Consequently, a large amount of oxygen vacancies may accumulate on the catalyst surface of 15 wt % NiO/CeO_2 NR and modulate the CO_2 reforming process. The β peak of the H_2-TPR profile for 15 wt % NiO/CeO_2 NR corresponds with these observations. Figure 5c,f demonstrate the XPS spectra of Ni 2p for 5 wt % NiO/CeO_2 NR and 15 wt % NiO/CeO_2 NR, respectively. The multi-split peaks at BE = 863.2 and 861.6 eV and the satellite at 868.7 eV are attributed to Ni $2p_{3/2}$ which determine the Ni^{3+} and Ni^{2+} concentration. The higher concentration of NiO on CeO_2 increases the proportion of Ce^{3+} present on the 15 wt % NiO/CeO_2 NR catalyst. Thus, the amount of NiO doping is shown to have a substantial effect on charge imbalance, defects, and oxygen vacancy density, all of which are also confirmed by the RAMAN profile (Figure S3) and promote DRM reaction activation.

3.4. Transmission Electron Microscopy. Figure 6 shows low- and high-magnification TEM images of the CeO_2 NR-supported 15 wt % NiO catalyst, as well as the selected area electron diffraction (SAED) pattern of CeO_2 and NiO. It is evident that the CeO_2 shape remains unchanged after NiO loading and calcination. The length and diameter of the CeO_2 NRs are in the ranges of 60−80 and 5−10 nm, respectively. The SAED patterns in Figure 6b,c exhibit four well-defined diffraction rings for CeO_2 and one diffraction ring for the NiO crystal. These rings correspond to the (111), (200), (220), and (311) crystalline planes of CeO_2, along with the (200) crystalline plane of NiO. The *d*-spacing value of 0.301 nm demonstrated by CeO_2 corresponds to the (111) plane, while the *d*-spacing value of 0.207 nm shown by NiO corresponds to the (200) plane. The same crystalline plane was observed in the lattice fringes of the TEM images. In Figure 6d, the HRTEM image clearly revealed the existence of lattice distortion and other defects.

4. RESULTS AND DISCUSSION

Figure 7 shows the molar fraction of CO_2, CH_4, CO, and H_2 obtained from QMS for DRM at eight different temperatures

Table 1. H_2 Consumption and Reduction Temperature of the Prepared Samples and Their Crystallite Size from the H_2-TPR Profiles and XRD Patterns

		reduction temperature (°C)			H_2 consumption (μmol g^{-1})		
samples	crystallite size (nm)	α_1	α_2	β	α	β	total surface H_2 consumption (μmol g^{-1})
5 wt % NiO/CeO_2 NR	8.74	174	236	290	8.45	7.77	16.22
15 wt % NiO/CeO_2 NR	7.41	180	244	314	2.96	26.59	29.55

https://doi.org/10.1021/acsami.3c09349
ACS Appl. Mater. Interfaces 2023, 15, 44984−44995

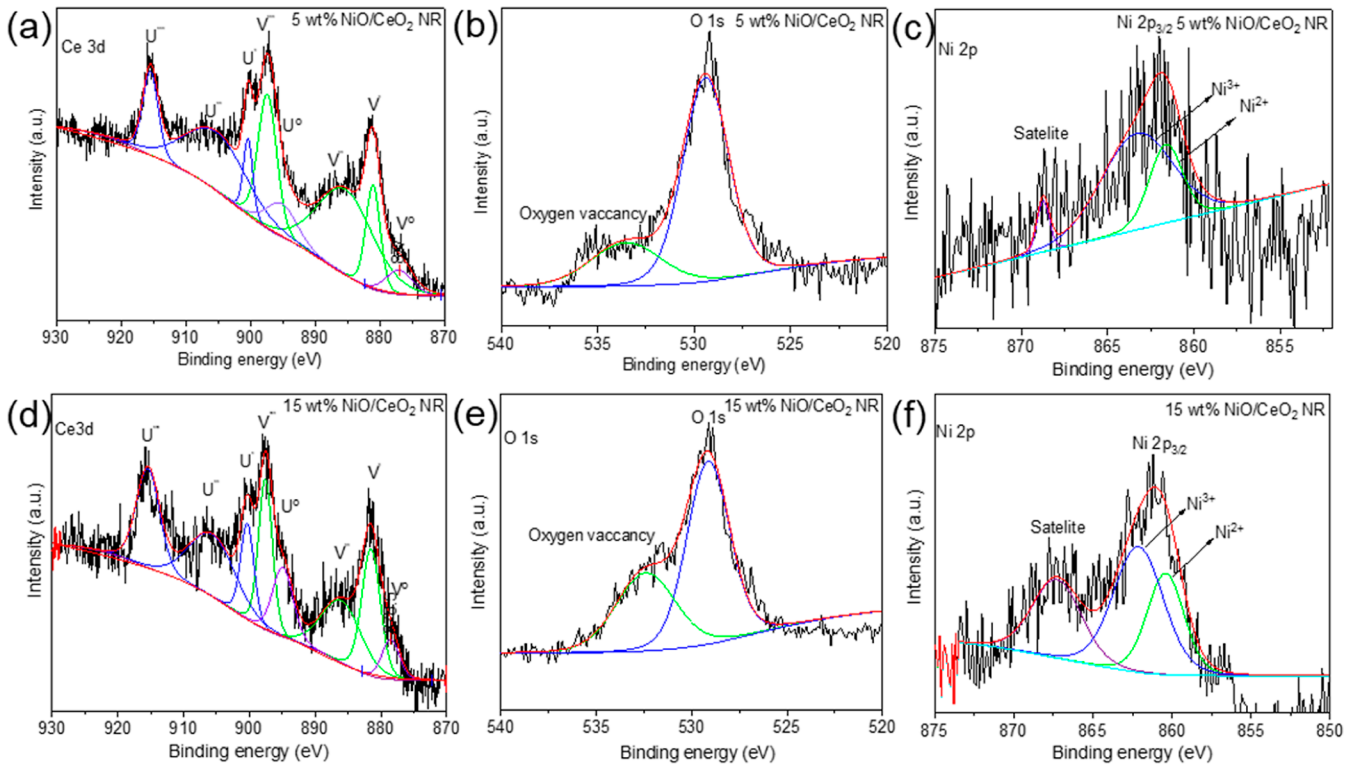

Figure 5. XPS spectra of Ce 3d, O 1s, and Ni 2p, respectively, for (a–c) 5 wt % NiO/CeO_2 NR and (d–f) 15 wt % NiO/CeO_2 NR.

ranging from 150 to 500 °C with 50 °C intervals for the 15 wt % NiO/CeO_2 NR catalyst. The plasma was introduced for 7 min, whereas thermal-only DRM was tested for 5 min. The thermal-only DRM was measured for the first 5 min, with the plasma starting on the 6th and stopping on the 12th minute. These two zones were distinguished in the figure by differently colored shading. The results from the introduction of plasma suggest that the thermodynamic barrier of DRM is easily surpassed, a phenomenon that is not possible with thermal-only DRM. For thermal catalytic DRM, no detectable CO and H_2 gases were observed for the first five min until the temperature reached 300 °C. However, with the initiation of plasma at the sixth minute, there were detectable 6% CO (red line) and 3% H_2 (sky-blue line) gases observed at temperatures as low as 150 °C, corresponding with a sudden decrease in mole concentration of CO_2 (black line) and CH_4 (blue line) in the exhaust gas. A small molar concentration of CO and H_2 was detected in the thermal catalysis region at 350 °C, with these concentrations increasing to 12 and 9%, respectively, at 500 °C. Comparatively, in the plasma catalytic region at 500 °C, there were 33 and 25% molar concentrations of CO and H_2, respectively. These results indicate that the introduction of plasma is crucial for initiating and promoting low-temperature DRM to produce syngas.

The conversion of the DRM reaction with only plasma, a plasma-assisted only CeO_2 NR support, a thermal-assisted catalyst, and a plasma-assisted catalyst is illustrated in Figure 8 for three different temperatures (350, 400, and 450 °C). Compared to thermally driven DRM, plasma-assisted DRM conversions are shown to occur at a much higher rate for both catalysts. In addition, neither catalyst showed any thermally assisted DRM reaction below 350 °C. Furthermore, the CH_4 and CO_2 conversion percentages with the plasma-only and CeO_2 NR-only conditions were less than 5%. It should be noted that the CH_4 conversion percentage was higher than the CO_2 conversion percentage in all circumstances, which can be attributed to the differences in bond energy. Due to the lower bond dissociation energy (BDE) of CH_4 (440 kJ/mol) compared to that of CO_2 (523 kJ/mol), the addition of plasma promotes more CH_4 conversion than CO_2[33]. In the case of thermally assisted DRM, the CH_4 is adsorbed on the Ni catalyst surface, which controls CH_4 conversion. Increasing the Ni content (from 5 to 15 wt %) consequently increases CH_4 conversion.

4.1. Conversion of Input Gases and Efficiency of Syngas Production. The performance of the NiO catalyst on CeO_2 NR support for DRM application in a NTP environment was investigated at temperatures ranging from 150 to 500 °C with a total flow rate of 350 sccm (CH_4: CO_2 molar ratio = 100:250 sccm) without inert gas dilution. The experimentally observed DRM effect for various temperatures is shown in Figures 9 and 10.

Figure 9 represents the experimentally obtained conversion of CH_4 and CO_2 for both pure thermal- and plasma-assisted DRM experiments across a range of temperatures. When using the 5 wt % NiO/CeO_2 NR catalyst, the CH_4 conversion rate ranges from 5%–15% (pure thermal) and 14–50% (plasma-thermal synergy) over the temperature range of 150–500 °C. At the same temperature range, the CH_4 conversion rate is 8–29% (pure thermal) and 21–66% (plasma-thermal synergy) when using the 15 wt % NiO/CeO_2 NR catalyst. On the other hand, CO_2 conversion changes from 3 to 13% (pure thermal) and 10 to 40% (plasma-thermal synergy) for the 5 wt % NiO/CeO_2 NR catalyst and from 3–24% (pure thermal) to 15–48% (plasma-thermal synergy) for the 15 wt % NiO/CeO_2 NR catalyst. The plasma-assisted DRM began converting gases at temperatures as low as 150 °C, whereas the thermal DRM began working at roughly 350 °C. It is also noticeable that the

https://doi.org/10.1021/acsami.3c09349
ACS Appl. Mater. Interfaces 2023, 15, 44984–44995

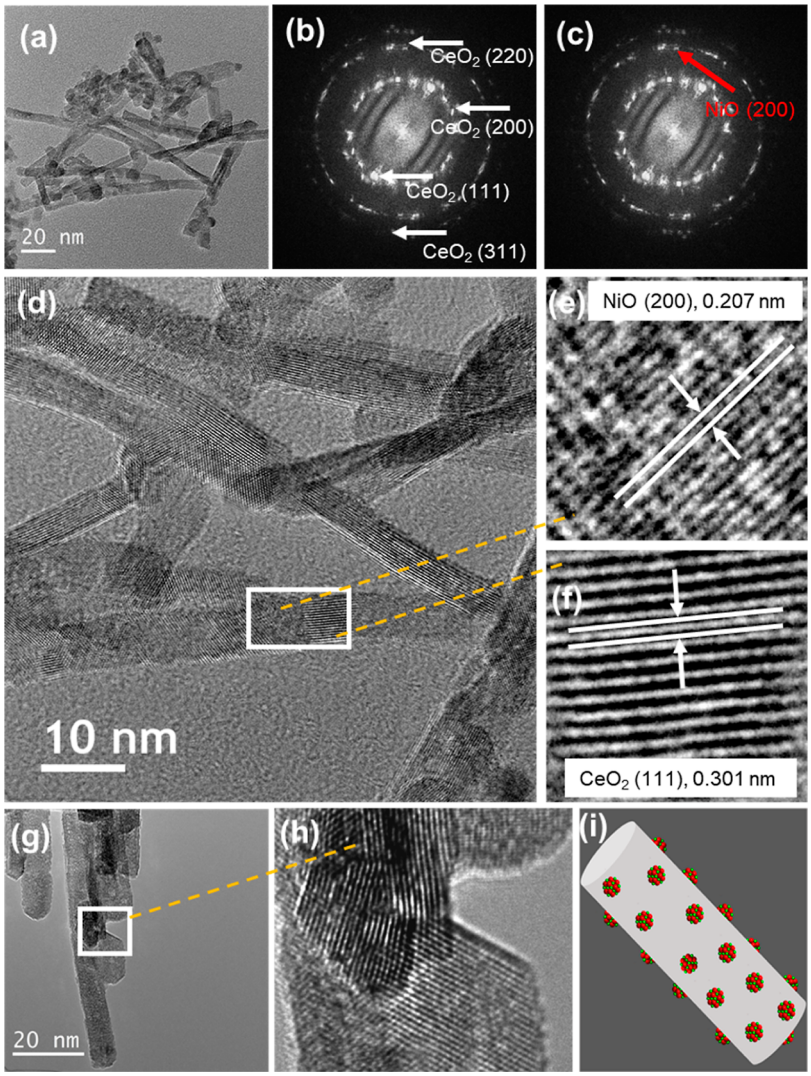

Figure 6. (a,d,g,h) HRTEM images of 15 wt % NiO/CeO_2 NR with different magnification, (b,c) SAED patterns of 15 wt % NiO/CeO_2 NR, (e,f) *d* spacing of NiO and CeO_2, and (i) NiO-coated CeO_2 catalyst model.

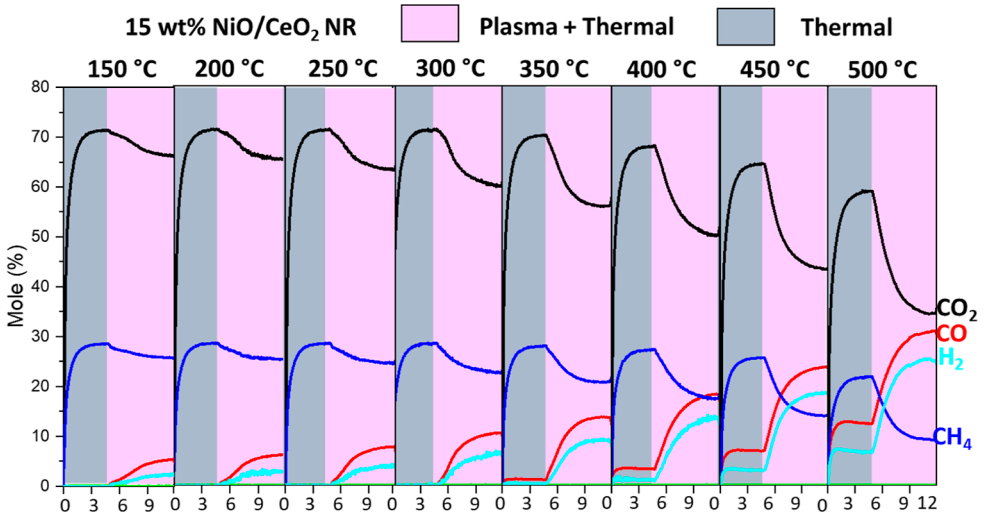

Figure 7. Measured time-resolved species mole fraction for thermal and thermal + plasma regions from 150 to 500 °C, 1 atm pressure (5 min for thermal catalysis only and 7 min for thermal + plasma catalysis) (catalyst wt: ∼200 mg, power: 24.9−25.8 W, frequency: 20 kHz, flow rate: CO_2: 250 sccm and CH_4: 100 sccm).

https://doi.org/10.1021/acsami.3c09349
ACS Appl. Mater. Interfaces 2023, 15, 44984−44995

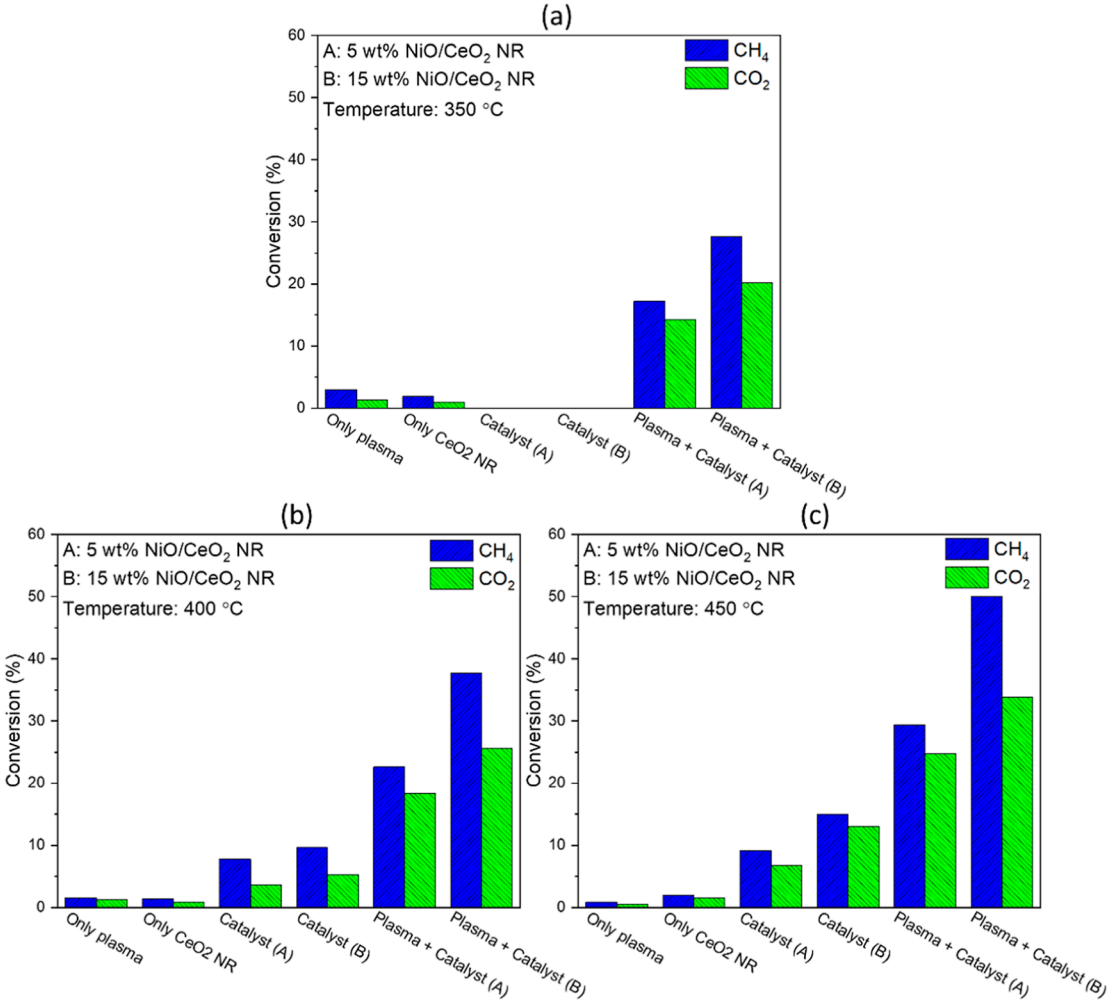

Figure 8. Comparison of CO_2 and CH_4 conversion in only plasma, only plasma + support (CeO_2 NR), thermal-assisted DRM with catalysts, and plasma-assisted DRM with catalysts for three different temperatures: (a) 350, (b) 400, and (c) 450 °C (catalyst wt: ∼200 mg, power: 24.9−25.8 W, frequency: 20 kHz, flow rate: CO_2: 250 sccm and CH_4: 100 sccm).

CO_2 conversion percentage is comparatively lower than the CH_4 conversion percentage. As was previously mentioned, the plasma aids in breaking down CH_4 more readily than CO_2 since CH_4 has a smaller BDE than CO_2, which increases its adsorption on NiO surfaces, hence enhancing CH_4 conversion. Additionally, the quantity of Ni present in the catalyst and the lower supply of CH_4 relative to that of CO_2 can be seen as factors influencing this result. As NiO adsorbs CH_4, a catalyst with a higher Ni content (15 wt % in this case) absorbs and breaks down more CH_4 than a catalyst with a lower Ni content (5 wt %), resulting in a greater CH_4 conversion rate. Others have previously investigated the effect of smaller CH_4/CO_2 molar ratios on thermal DRM using Ni−CeO_2/MgO,[13] Ni-WC, and Ni−Mo_2C.[34] They discovered that, for thermal DRM, CH_4 conversion is higher when the CH_4/CO_2 molar ratio is less than unity, which could be attributed to an excess amount of CO_2. In another research review,[35] the authors noted that the presence of a higher CO_2 concentration increases CH_4 conversions in plasma catalytic synergy. According to their hypothesis, the plasma zone produces methyl/hydrocarbon radicals from CH_4 due to reactive metastable $O(^1D)$ produced by CO_2 dissociation, thus allowing the cofeed to promote each other's conversions.

According to our investigation, the 15 wt % NiO/CeO_2 NR catalyst demonstrated the highest CH_4 and CO_2 conversion rates, which were 29 and 24%, respectively, for thermal DRM, and 67 and 48%, respectively, for plasma-assisted DRM. It is obvious that the plasma contribution enhanced the conversion rate by more than doubling it. The conversion rates for plasma thermal synergy employing our shaped 15 wt % NiO/CeO_2 NR catalyst are higher compared to those of other catalysts tested in different plasma environments. When compared to experiments employing nearly equal feed ratios and different Ni-based catalysts such as Ni/γ-Al_2O_3 in a DBD reactor,[30] x-Ni/γ-Al_2O_3 (x = 5, 10, 20) in a corona discharge reactor,[31] x-Ni/Al_2O_3 (x = 15, 30) in a rotating gliding spouted bed reactor, structural and textural modified CaO,[8] and 15 wt % Ni/TiO_2,[32] higher conversion rates were achieved by our shaped 15 wt % NiO/CeO_2 NR catalyst. Although certain conversions are possible at temperatures as low as 150 °C, the plasma thermal synergy effect becomes the most effective between 300 and 500 °C. The 15 wt % NiO/CeO_2 NR catalyst performs similarly to lanthanum-based catalysts with aluminum supports such as $LaNiO_3$/γ-Al_2O_3[36] and La−Ni/γ-Al_2O_3[37] under almost identical circumstances and reaction environments.

https://doi.org/10.1021/acsami.3c09349
ACS Appl. Mater. Interfaces 2023, 15, 44984−44995

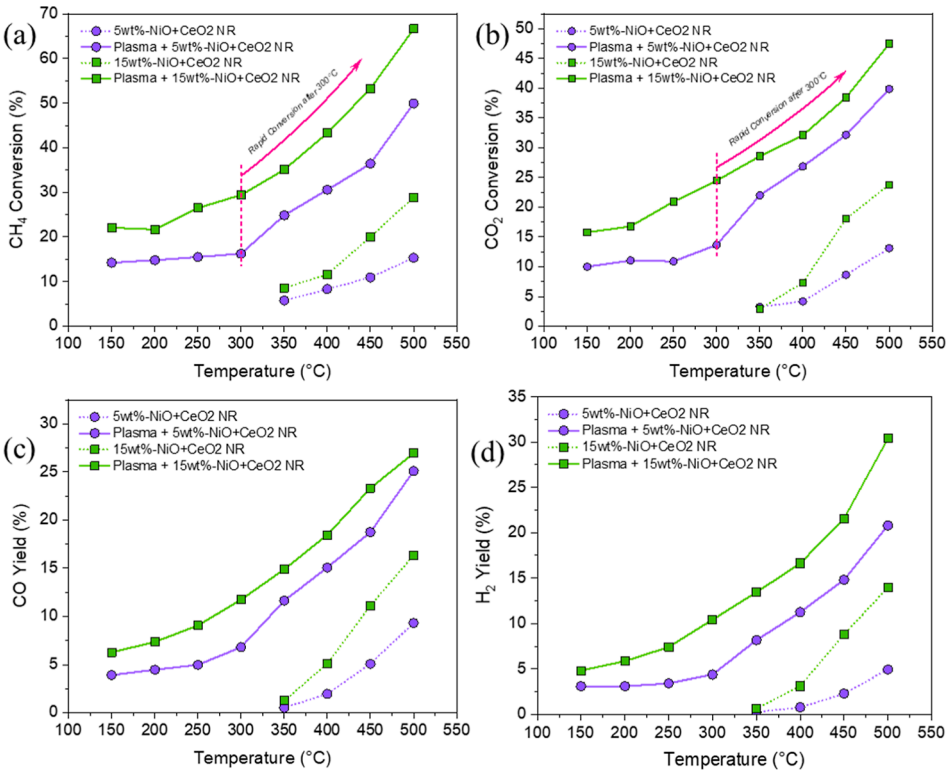

Figure 9. (a) CH_4 conversion, (b) CO_2 conversion, (c) CO yield, and (d) H_2 yield using the 5 wt % NiO/CeO_2 NR and 15 wt % NiO/CeO_2 NR catalysts at various temperatures (catalyst wt: ∼200 mg, power: 24.9−25.8 W, frequency: 20 kHz, flow rate: CO_2: 250 sccm and CH_4: 100 sccm).

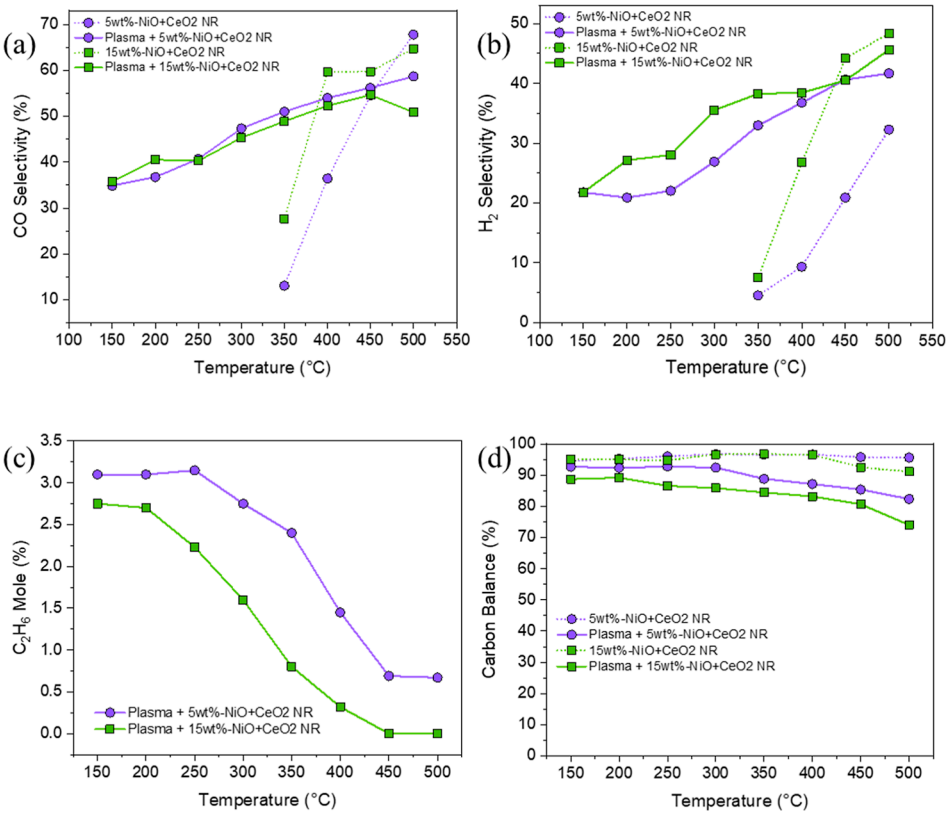

Figure 10. (a) CO selectivity, (b) H_2 selectivity, (c) C_2H_6 production, and (d) carbon balances for the 5 wt % NiO/CeO_2 NR and 15 wt % NiO/CeO_2 NR catalysts at various temperatures (catalyst wt: ∼200 mg, power: 24.9−25.8 W, frequency: 20 kHz, flow rate: CO_2: 250 sccm and CH_4: 100 sccm).

https://doi.org/10.1021/acsami.3c09349
ACS Appl. Mater. Interfaces 2023, 15, 44984−44995

The yields of CO and H_2 as a function of temperature for both thermal- and plasma-assisted catalysis methods are shown in Figure 9c,d. The yields are proportional to temperature, with the maximum yields of 27% for CO and 31% for H_2 achieved at 500 °C when plasma is applied onto the 15 wt % NiO/CeO_2 NR catalyst. The results also show that the 5 wt % NiO/CeO_2 NR catalyst is more effective at producing CO than H_2, while the 15 wt % NiO/CeO_2 NR catalyst produces H_2 more effectively than CO. However, in the thermal DRM scenario, both catalysts produce CO more effectively than H_2. The addition of plasma to the experiment increases the quantity of CH_4 conversion, which, in turn, increases the amount of H_2 produced.

Figure 10a,b illustrates the trends in CO and H_2 selectivity, which reflect the formation of the desired CO and H_2 to the formation of secondary products. At 500 °C, pure thermal DRM achieves its maximum selectivity with values for CO and H_2 of 68 and 49%, respectively. In the case of plasma-assisted DRM, selectivity increases with increasing temperature, indicating that the process moves in the direction of the DRM reaction (eq 1). At lower temperatures, the plasma breaks down CH_4 into more CH_x^+ (x = 1, 2) radicals than H^+ radicals, leading to the generation of C_2 hydrocarbons (C_2H_6 in this instance) rather than H_2, which lowers the selectivity. On the other hand, when the temperature rises, the Ni catalyst becomes more active, able to adsorb gaseous C_2H_6 on the surface and dissociate bonds via ethane cracking (eqs 10 and 11) or the ethane dry reforming process (eq 12), increasing the selectivity.[38] This claim is also verified by the C_2H_6 production shown in Figure 10c, which depicts the reduction in C_2H_6 formation with increasing temperature. The responsible Ni through adsorption slows down the production of C2 hydrocarbons, causing the formation rate of C_2H_6 to be comparably lower for 15 wt % NiO/CeO_2 NR (higher Ni content) than for 5 wt % NiO/CeO_2 NR (lower Ni content). The carbon balance in Figure 10d depicts the variation in the production of unwanted carbonaceous products and carbon deposition with temperature. As temperature rises, kinetic energy increases and dissociation energy decreases, and the plasma is able to break more bonds. This results in carbon deposition through CH_4 breakdown (eq 2) and CO desorption (eq 3). In both thermal- and plasma-assisted DRM, 15 wt % NiO/CeO_2 NR deposits more carbon than 5 wt % NiO/CeO_2 NR because the amount of Ni in the catalyst is directly related to the rate of carbon deposition. Finally, the SMSI of the 15 wt % NiO/CeO_2 NR catalyst produces a large number of oxygen vacancies, which improves the performance.

$$C_2H_6(g) = 2C(s) + 3H_2(g) \quad (10)$$

$$C_2H_6(g) + H_2(g) = 2CH_4(g) \quad (11)$$

$$C_2H_6(g) + 2CO_2(g) = 4CO(g) + 3H_2(g) \quad (\Delta H_{298K} = +428.1\text{kJ mol}^{-1}) \quad (12)$$

5. CONCLUSIONS

In summary, NTP-assisted catalytic DRM is considered an efficient approach for converting CO_2 and CH_4 to valuable chemicals and fuels. The prepared catalysts were analyzed qualitatively and quantitatively using XRD, H_2-TPR, HRTEM, and XPS. The catalytic evaluation showed that the 15 wt % NiO/CeO_2 NR catalyst significantly improves the DRM conversion compared to the 5 wt % NiO/CeO_2 NR catalyst. In addition, introducing NTP facilitates the conversion far more effectively than conventional thermal catalysis DRM. H_2-TPR, XPS, and CO_2 TPD profiles of catalysts confirmed that an increase in NiO loading over CeO_2 NR support enhanced the oxygen vacancy density of the catalysts by replacing Ce^{4+} with Ni^{2+} ions. This method was shown to promote higher conversion, up to 66% for CH_4 and 49% for CO_2 at 500 °C.

■ ASSOCIATED CONTENT

Supporting Information

The Supporting Information is available free of charge at https://pubs.acs.org/doi/10.1021/acsami.3c09349.

Additional material characterization and performance measurement details for the 5 and 15 wt % CeO_2 NR-supported NiO catalysts, including CO_2/CO-TPD profiles, Raman spectroscopy, Rietveld analysis, power and temperature measurement of the reactor, and activation energy graph (PDF)

■ AUTHOR INFORMATION

Corresponding Author

Ruigang Wang − *Department of Metallurgical and Materials Engineering, The University of Alabama, Tuscaloosa, Alabama 35487, United States;* orcid.org/0000-0002-0678-7460; Email: rwang@eng.ua.edu

Authors

Md Robayet Ahasan − *Department of Metallurgical and Materials Engineering, The University of Alabama, Tuscaloosa, Alabama 35487, United States*

Md Monir Hossain − *Department of Metallurgical and Materials Engineering, The University of Alabama, Tuscaloosa, Alabama 35487, United States*

Zephyr Barlow − *Department of Metallurgical and Materials Engineering, The University of Alabama, Tuscaloosa, Alabama 35487, United States*

Xiang Ding − *College of Urban and Environmental Sciences, Peking University, Beijing 100871, China*

Complete contact information is available at: https://pubs.acs.org/10.1021/acsami.3c09349

Notes

The authors declare no competing financial interest.

■ ACKNOWLEDGMENTS

This work was supported by the National Science Foundation (CBET-1856729 and TI-2044733). This project also received partial financial support from the Alabama Transportation Institute and Alabama Water Institute. The use of electron microscopy facilities at the Alabama Analytical Research Center (AARC), The University of Alabama, is gratefully acknowledged.

■ REFERENCES

(1) Martin-del-Campo, J.; Uceda, M.; Coulombe, S.; Kopyscinski, J. Plasma-Catalytic Dry Reforming of Methane over Ni-Supported Catalysts in a Rotating Gliding Arc-Spouted Bed Reactor. *J. CO2 Util.* **2021**, *46*, 101474.

(2) Brune, L.; Ozkan, A.; Genty, E.; Visart de Bocarmé, T.; Reniers, F. Dry Reforming of Methane via Plasma-Catalysis: Influence of the Catalyst Nature Supported on Alumina in a Packed-Bed DBD Configuration. *J. Phys. D Appl. Phys.* **2018**, *51* (23), 234002.

(3) Zeng, Y.; Zhu, X.; Mei, D.; Ashford, B.; Tu, X. Plasma-Catalytic Dry Reforming of Methane over γ-Al2O3 Supported Metal Catalysts. *Catal. Today* **2015**, *256*, 80−87.
(4) Kim, S.-S.; Kwon, B.; Kim, J. Plasma Catalytic Methane Conversion over Sol-Gel Derived Ru/TiO2 Catalyst in a Dielectric-Barrier Discharge Reactor. *Catal. Commun.* **2007**, *8* (12), 2204−2207.
(5) Elsayed, N. H.; Roberts, N. R. M.; Joseph, B.; Kuhn, J. N. Low Temperature Dry Reforming of Methane over Pt-Ni-Mg/Ceria-Zirconia Catalysts. *Appl. Catal., B* **2015**, *179*, 213−219.
(6) Khoja, A. H.; Tahir, M.; Amin, N. A. S. Cold Plasma Dielectric Barrier Discharge Reactor for Dry Reforming of Methane over Ni/γ-Al2O3-MgO Nanocomposite. *Fuel Process. Technol.* **2018**, *178*, 166−179.
(7) Wang, Y.; Yao, L.; Wang, S.; Mao, D.; Hu, C. Low-Temperature Catalytic CO2 Dry Reforming of Methane on Ni-Based Catalysts: A Review. *Fuel Process. Technol.* **2018**, *169*, 199−206.
(8) Kim, S. B.; Eissa, A. A.-S.; Kim, M.-J.; Goda, E. S.; Youn, J.-R.; Lee, K. Sustainable Synthesis of a Highly Stable and Coke-Free Ni@CeO2 Catalyst for the Efficient Carbon Dioxide Reforming of Methane. *Catalysts* **2022**, *12* (4), 423.
(9) Yan, X.; Hu, T.; Liu, P.; Li, S.; Zhao, B.; Zhang, Q.; Jiao, W.; Chen, S.; Wang, P.; Lu, J.; et al. Highly Efficient and Stable Ni/CeO2-SiO2 Catalyst for Dry Reforming of Methane: Effect of Interfacial Structure of Ni/CeO2 on SiO2. *Appl. Catal., B* **2019**, *246*, 221−231.
(10) Ahasan, M. R.; Wang, Y.; Wang, R. In Situ DRIFTS and CO-TPD Studies of CeO2 and SiO2 Supported CuOx Catalysts for CO Oxidation. *Mol. Catal.* **2022**, *518*, 112085.
(11) Rui, N.; Zhang, X.; Zhang, F.; Liu, Z.; Cao, X.; Xie, Z.; Zou, R.; Senanayake, S. D.; Yang, Y.; Rodriguez, J. A.; Liu, C.-J. Highly Active Ni/CeO2 Catalyst for CO2Methanation: Preparation and Characterization. *Appl. Catal., B* **2021**, *282*, 119581.
(12) Tuti, S.; Luisetto, I.; Pasqual Laverdura, U.; Marconi, E. Dry Reforming of Methane on Ni/Nanorod-CeO2 Catalysts Prepared by One-Pot Hydrothermal Synthesis: The Effect of Ni Content on Structure, Activity, and Stability. *Reactions* **2022**, *3* (3), 333−351.
(13) Khajenoori, M.; Rezaei, M.; Meshkani, F. Dry Reforming over CeO2-Promoted Ni/MgO Nano-Catalyst: Effect of Ni Loading and CH4/CO2Molar Ratio. *J. Ind. Eng. Chem.* **2015**, *21*, 717−722.
(14) Afzal, S.; Prakash, A. V.; Littlewood, P.; Marks, T. J.; Weitz, E.; Stair, P. C.; Elbashir, N. O. Controlling the Rate of Change of Ni Dispersion in Commercial Catalyst by ALD Overcoat during Dry Reforming of Methane. *Int. J. Hydrogen Energy* **2020**, *45* (23), 12835−12848.
(15) Malwadkar, S.; Bera, P.; Hegde, M. S.; Satyanarayana, C. V. V. Preferential Oxidation of CO on Ni/CeO 2 Catalysts in the Presence of Excess H 2 and CO 2. *React. Kinet. Mech. Catal.* **2012**, *107* (2), 405−419.
(16) Wei, Z.; Wang, R. Chemically Etched CeO2-x Nanorods with Abundant Surface Defects as Effective Cathode Additive for Trapping Lithium Polysulfides in Li-S Batteries. *J. Colloid Interface Sci.* **2022**, *615*, 527−542.
(17) Ranganathan, R. V.; Hossain, M. M.; Talukdar, S.; Ahasan, R.; Wang, R.; Uddi, M. Tunable Quantum Cascade Laser Absorption Spectroscopy for Plasma Assisted Oxidative Coupling of Methane to C 2 Based Products. In *2021 IEEE International Conference on Plasma Science (ICOPS)*; IEEE, 2021; p 1.
(18) Du, X.; Zhang, D.; Shi, L.; Gao, R.; Zhang, J. Morphology Dependence of Catalytic Properties of Ni/CeO2 Nanostructures for Carbon Dioxide Reforming of Methane. *J. Phys. Chem. C* **2012**, *116* (18), 10009−10016.
(19) Zhao, P.; Qin, F.; Huang, Z.; Sun, C.; Shen, W.; Xu, H. Morphology-Dependent Oxygen Vacancies and Synergistic Effects of Ni/CeO 2 Catalysts for N 2 O Decomposition. *Catal. Sci. Technol.* **2018**, *8* (1), 276−288.
(20) Sudarsanam, P.; Hillary, B.; Mallesham, B.; Rao, B. G.; Amin, M. H.; Nafady, A.; Alsalme, A. M.; Reddy, B. M.; Bhargava, S. K. Designing CuO_x Nanoparticle-Decorated CeO_2 Nanocubes for Catalytic Soot Oxidation: Role of the Nanointerface in the Catalytic Performance of Heterostructured Nanomaterials. *Langmuir* **2016**, *32* (9), 2208−2215.
(21) Abbas, F.; Jan, T.; Iqbal, J.; Ahmad, I.; Naqvi, M. S. H.; Malik, M. Facile Synthesis of Ferromagnetic Ni Doped CeO2 Nanoparticles with Enhanced Anticancer Activity. *Appl. Surf. Sci.* **2015**, *357*, 931−936.
(22) Deraz, N. M. Effect of NiO Content on Structural, Surface and Catalytic Characteristics of Nano-Crystalline NiO/CeO2 System. *Ceram. Int.* **2012**, *38* (1), 747−753.
(23) Mock, S. A.; Zell, E. T.; Hossain, S. T.; Wang, R. Effect of Reduction Treatment on CO Oxidation with CeO_2 Nanorod-Supported CuO_x Catalysts. *ChemCatChem* **2018**, *10* (1), 311−319.
(24) Peymani, M.; Alavi, S. M.; Arandiyan, H.; Rezaei, M. Rational Design of High Surface Area Mesoporous Ni/CeO2 for Partial Oxidation of Propane. *Catalysts* **2018**, *8* (9), 388.
(25) Jomjaree, T.; Sintuya, P.; Srifa, A.; Koo-amornpattana, W.; Kiatphuengporn, S.; Assabumrungrat, S.; Sudoh, M.; Watanabe, R.; Fukuhara, C.; Ratchahat, S. Catalytic Performance of Ni Catalysts Supported on CeO2 with Different Morphologies for Low-Temperature CO2Methanation. *Catal. Today* **2021**, *375*, 234−244.
(26) Wang, L.; Liu, H.; Liu, Y.; Chen, Y.; Yang, S. Influence of Preparation Method on Performance of Ni-CeO2 Catalysts for Reverse Water-Gas Shift Reaction. *J. Rare Earths* **2013**, *31* (6), 559−564.
(27) Bendieb Aberkane, A.; Yeste, M. P.; Fayçal, D.; Goma, D.; Cauqui, M. A. Catalytic Soot Oxidation Activity of NiO-CeO2 Catalysts Prepared by a Coprecipitation Method: Influence of the Preparation Ph on the Catalytic Performance. *Materials* **2019**, *12* (20), 3436.
(28) Ratchahat, S.; Surathitimethakul, S.; Thamungkit, A.; Mala, P.; Sudoh, M.; Watanabe, R.; Fukuhara, C.; Chen, S. S.; Wu, K. C.-W.; Charinpanitkul, T. Catalytic Performance of Ni/CeO2 Catalysts Prepared from Different Routes for CO2Methanation. *J. Taiwan Inst. Chem. Eng.* **2021**, *121*, 184−196.
(29) Tada, S.; Nagase, H.; Fujiwara, N.; Kikuchi, R. What Are the Best Active Sites for CO2Methanation over Ni/CeO2? *Energy Fuels* **2021**, *35* (6), 5241−5251.
(30) Lin, S.; Hao, Z.; Shen, J.; Chang, X.; Huang, S.; Li, M.; Ma, X. Enhancing the CO2Methanation Activity of Ni/CeO2 via Activation Treatment-Determined Metal-Support Interaction. *J. Energy Chem.* **2021**, *59*, 334−342.
(31) Rana, A. M.; Akbar, T.; Ismail, M.; Ahmad, E.; Hussain, F.; Talib, I.; Imran, M.; Mehmood, K.; Iqbal, K.; Nadeem, M. Y. Endurance and Cycle-to-Cycle Uniformity Improvement in Tri-Layered CeO2/Ti/CeO2 Resistive Switching Devices by Changing Top Electrode Material. *Sci. Rep.* **2017**, *7* (1), 39539.
(32) Mofarah, S.; Adabifiroozjaei, E.; Yao, Y.; Koshy, P.; Lim, S.; Webster, R.; Liu, X.; Khayyam Nekouei, R.; Cazorla, C.; Liu, Z.; Wang, Y.; Lambropoulos, N.; Sorrell, C. C. Proton-Assisted Creation of Controllable Volumetric Oxygen Vacancies in Ultrathin CeO2-x for Pseudocapacitive Energy Storage Applications. *Nat. Commun.* **2019**, *10* (1), 2594.
(33) Luo, Y.-R. *Comprehensive Handbook of Chemical Bond Energies*; CRC Press, 2007.
(34) Barbosa, R. D.; Baldanza, M. A. S.; de Resende, N. S.; Passos, F. B.; da Silva, V. L. d. S. T. Nickel-Promoted Molybdenum or Tungsten Carbides as Catalysts in Dry Reforming of Methane: Effects of Variation in CH4/CO2Molar Ratio. *Catal. Lett.* **2021**, *151* (6), 1578−1591.
(35) Istadi; Amin, N. A. S. Co-Generation of Synthesis Gas and C2+ Hydrocarbons from Methane and Carbon Dioxide in a Hybrid Catalytic-Plasma Reactor: A Review. *Fuel* **2006**, *85* (5−6), 577−592.
(36) Zheng, X.-G.; Tan, S.-Y.; Dong, L.-C.; Li, S.-B.; Chen, H.-M.; Wei, S.-A. Experimental and Kinetic Investigation of the Plasma Catalytic Dry Reforming of Methane over Perovskite LaNiO3 Nanoparticles. *Fuel Process. Technol.* **2015**, *137*, 250−258.
(37) Li, J.; Xu, B.; Wang, W.; Xie, J.; Yin, X.; Wu, C.; Xiao, J. Experimental Study on Dry Reforming of Methane by a Plasma

https://doi.org/10.1021/acsami.3c09349
ACS Appl. Mater. Interfaces 2023, 15, 44984−44995

Catalytic Hybrid System. *J. Fuel Chem. Technol.* **2021**, *49* (8), 1161−1172.
(38) Tsiotsias, A. I.; Charisiou, N. D.; Sebastian, V.; Gaber, S.; Hinder, S. J.; Baker, M. A.; Polychronopoulou, K.; Goula, M. A. A Comparative Study of Ni Catalysts Supported on Al2O3, MgO-CaO-Al2O3 and La2O3-Al2O3 for the Dry Reforming of Ethane. *Int. J. Hydrogen Energy* **2022**, *47* (8), 5337−5353.

https://doi.org/10.1021/acsami.3c09349
ACS Appl. Mater. Interfaces 2023, 15, 44984−44995